Time dependence of advection-diffusion coupling for nanoparticle ensembles

Alexandre Vilquin,[1] Vincent Bertin,[1, 2] Pierre Soulard,[1] Gabriel Guyard,[1, 3]
Elie Raphaël,[1] Frédéric Restagno,[3] Thomas Salez,[2, 4] and Joshua D. McGraw[1]

[1]*Gulliver CNRS UMR 7083, PSL Research University,*
ESPCI Paris, 10 rue Vauquelin, 75005 Paris, France
[2]*Univ. Bordeaux, CNRS, LOMA, UMR 5798, F-33405, Talence, France*
[3]*Universit Paris-Saclay, CNRS, Laboratoire de physique des solides, Orsay, France*
[4]*Global Station for Soft Matter, Global Institution for Collaborative*
Research and Education, Hokkaido University, Sapporo, Hokkaido, Japan
(Dated: July 17, 2020)

Particle transport in fluids at micro- and nano-scales is important in many domains. As compared to the quiescent case, the time evolution of particle dispersion is enhanced by coupling: *i*) advection along the flow; and *ii*) diffusion along the associated velocity gradients. While there is a well-known, long-time limit for this advection-diffusion enhancement, understanding the short-time limit and corresponding crossover between these two asymptotic limits is less mature. We use evanescent-wave video microscopy for its spatio-temporal resolution. Specifically, we observe a near-surface zone of where the velocity gradients, and thus dispersion, are the largest within a simple microfluidic channel. Supported by a theoretical model and simulations based on overdamped Langevin dynamics, our experiments reveal the crossover of this so-called Taylor dispersion from short to long time scales. Studying a range of particle size, viscosity and applied pressure, we show that the initial spatial distribution of particles can strongly modify observed master curves for short-time dispersion and its crossover into the long-time regime.

PACS numbers:

Hydrodynamic flows typically exhibit a spatially varying velocity, often as a result of a nearby solid, immobile boundary. When microscopic particles are transported by such a near-surface flow, the coupling between diffusion along the flow gradients and streamwise advection leads to an enhanced dispersion as compared to the no-flow case. This enhancement was first quantitatively described by G.I. Taylor [1] for laminar flows in a cylindrical tube. These predictions were particularly applicable to times long compared to the one over which a particle diffuses across the width of the tube, here called the Taylor time. From this foundational work, and in a strict analogy to simple Fickian diffusion, a dispersion coefficient could be identified as half the variance of the solute displacement divided by the time; the latter being quadratic in the typical flow speed. Taylor's description was formalised in this laminar tube-flow context by Aris [2], generalised by Brenner and others [3–6], and eventually used to measure diffusion coefficients [7] and influences lab-on-chip design [8].

Such a mature theoretical description of the dispersion complemented with experiments is not available for times short compared to the Taylor time. Nevertheless, several theoretical works [9–13], and some more recent experiments [14–16] were devoted to this short-time limit. These results demonstrate that the dispersion coefficient quadratically increases with time for single-particle observations. However, it is often the case that an ensemble of particles is released from a particular region and their spatio-temporal evolution should be known in detail. Drug delivery from a suddenly rup-

tured nanoparticle [17, 18] provides just one microscopic example. More generally, the efficacy of nanoconfined chemical reactions [19, 20] should critically depend on the time-dependent spatial distribution of reactants. Besides, Taylor dispersion also plays an important role in pulmonary air exchanges [21, 22], the mixing of cerebrospinal fluids [23], DNA molecular mobility [24] and other contexts at the micro- and nano-scales [25–28].

Among the experiments capable of quantitatively accessing short- and long-time dispersion at the nanoscale is total internal reflection fluorescence microscopy (TIRFM). Initially developed for near-surface cell biology [29, 30], TIRFM illuminates a sample with an evanescent wave decaying exponentially from the surface as shown schematically in Fig. 1(a). TIRFM was particularly used to study near-surface colloid/surface interactions in equilibrium [31], following which nanovelocimetry was implemented [32–36], allowing for the quantitative characterization of slip boundary conditions at the nanoscale [32, 37–39], and to study hindered diffusion near a solid/liquid interface [40].

Here we use TIRFM to examine the dispersion of nanoparticle ensembles for a broad range of timescales in a linear shear flow, as shown schematically in Figs. 1(a) and (b). We first demonstrate the quadratic shear-rate dependence of the dispersion coefficient for a linear flow profile. We then study the time dependence, where for short-times the dispersion coefficient increases with time before reaching a long-time plateau predicted using the Taylor method. We find that the transient regime is strongly affected by the grouping of particles: *i*) in

the most general case a mixed-power time dependence is observed for the dispersion coefficient; *ii*) a corresponding linear time dependence can be observed for all-channel, simple-shear protocols; and *iii*) the pure, quadratic time dependence of the dispersion coefficient can be approached by selecting particles in the finest range of altitudes available to the experiment. Analytical modelling allows us to capture the asymptotic behaviours —including an early-time linear-to-quadratic crossover— while Langevin simulations are used to quantitatively recover the full experimental dynamics.

In our experiments —the details of which are found in the Materials and Methods, with the Supporting Information (SI) containing all notations— fluorescent nanoparticles with radius $a = 55$ or 100 nm were advected along the x-direction (*cf.* Fig. 1(b) and SI Video 1) of a pressure-driven flow. Pressure drops $5 \leq \Delta P \leq 400$ mbar were applied across rectangular microchannels with height, $h = 18$ μm, width $w = 180$ μm, and length, $\ell = 8.8$ cm. The fluid viscosities were $1 \leq \eta \leq 7.6$ mPa s, varied by controlling the concentration of glycerol/water mixtures. Given the exponentially decaying evanescent field, we call the apparent altitude $z = \Pi \ln(I_0/I)$ where Π is the exponential decay length, I is the measured particle intensity, as shown in Fig. 1(b), and I_0 is the fluorescence intensity at the wall. Optical aberrations lead to small deviations from an exact exponential decay for the fluorescence intensity, and such details are discussed in the SI. Comparing subsequent images, sample trajectories as in Fig. 1(b) and SI Video 2 were constructed using home-built Matlab routines.

The experimental setup allows the observation of particles in a range of altitudes $a \lesssim z \lesssim 1$ μm from the solid/liquid interface, the solid being a glass coverslip. Here $z = 0$ is set at the solid/liquid boundary and the camera sensitivity determines the upper z-limit. In practice, we do not observe particles for $z \lesssim 200$ nm as a result of electrostatic and steric interactions [31, 41, 42] (see SI for details). The near-surface flow has the advantage of simultaneously exhibiting the lowest velocities $(0 - 600$ μm s$^{-1})$ and largest shear rates $(100 - 600$ s$^{-1})$ as compared to the rest of the channel, offering pertinent conditions for studying the advection-diffusion coupling.

In order to obtain mean velocity profiles along the flow direction over a given lag time, τ, displacements, $\Delta x(z, \tau) = x(z, t + \tau) - x(z, t)$, were measured for each pair of frames for which an identical particle was detected, and taking t as the initial observation time (see Fig. 1(b)). Since the particle intensity encodes the altitude, we first sort the particles into a series of intensity bins, each bin corresponding to a range of approximately 15 nm. Then, the lag-time-independent (verified) streamwise mean velocity $v_x(\bar{z}) = \langle \Delta x(\bar{z}, \tau) \rangle / \tau$ is determined. Here, $\langle \cdot \rangle$ denotes ensemble averaging over *ca.* 10^5 particle observations for each experimental condition accessed for all t. The notation $\bar{\cdot}$ denotes averaging over
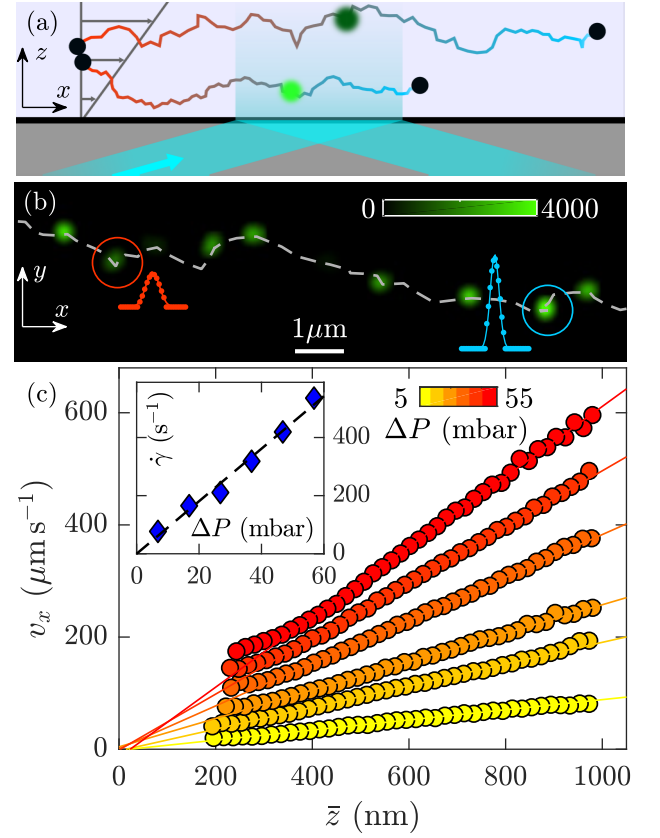

Figure 1: (a) Schematic of two Brownian colloids transported by a near surface shear flow in a microchannel illuminated by an evanescent wave. (b) Superposition of TIRFM images with lag time $\tau = 12.5$ ms, showing successive positions of a fluorescent 55 nm-radius nanoparticle. Two intensity profiles are shown (arbitrary units) with the red and blue dots fitted by Gaussian profiles. The dashed grey line is a guide to the eye. (c) Velocity profiles $v_x = \langle \Delta x \rangle / \tau$ for 55 nm-radius particles as observed in SI Videos 1 and 2 with a lag time $\tau = 2.5$ ms at several pressure drops. The plain lines indicate linear regressions, providing the shear rate value $\dot{\gamma}$. Inset: Shear rate as a function of pressure drop across the microfluidic channel. The dashed black line is a linear regression.

all frames during the lag time.

Figure 1(c) shows the streamwise velocity profiles for 55 nm-radius particles in water and several pressure drops. The solid lines show that the profiles are well approximated by linear functions (see SI and [35, 43] for a discussion of the small non-linearities). The spread of v_x-intercept values arises from the spread of values for I_0 at each pressure, $z = 0$ being taken as the mean of $\Pi \log I_0$ over the different ΔP; $z = 0$ is thus resolved to within 20 nm of the solid/liquid interface assuming no slip [35] as justified in the SI. The low Reynolds numbers (Re = $\rho h U/\eta \approx 10^{-2}$ with ρ the fluid density and U the average velocity in the whole channel) indicate a viscosity-dominated flow for which $v_x(\bar{z}) = \Delta P (\bar{z}^2 - h\bar{z})/2\eta L$, *i.e.* a Poiseuille flow. In the region $z \lesssim 1$ μm, and
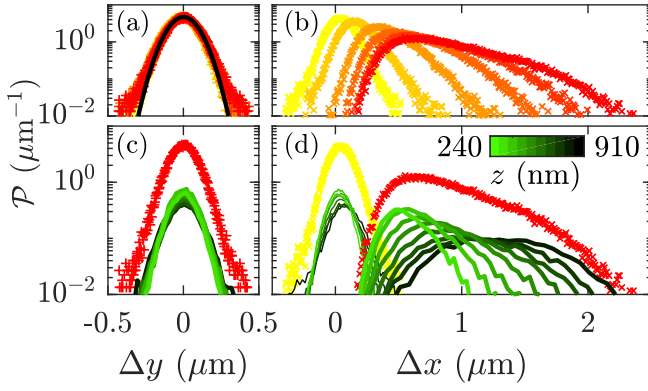
Figure 2: Probability density functions (PDFs) for all transverse (a) and streamwise (b) displacements measured for several pressure drops; the colour code corresponds to the one in Fig. 1(c). The black line in (a) indicates a Gaussian model $\mathcal{P}(\Delta y) = \exp\left(-\Delta y^2/2\sigma_{\Delta y}^2\right)/\sqrt{2\pi\sigma_{\Delta y}^2}$. In (c) the Δy-PDF for the largest pressure drop is decomposed into PDFs for several z. Each green-black PDF corresponds to a z-range of $ca.$ 30 nm (some curves omitted for clarity), and the mean value of z is indicated by the colour scale of (d). The decomposed Δx-PDFs for the smallest pressure drop (thinnest green-black lines) and the largest pressure drop (thickest green-black lines) are shown in (d). All the displacements are measured for a time lag $\tau = 2.5$ ms and concern 100 nm-radius particles in water.

given the channel height $h = 18\ \mu$m, the deviation of the Poiseuille profile from linearity is expected to be less than 5 %. Therefore, at first order in $\bar{z}/h$, we have $v_x(\bar{z}) \simeq \dot{\gamma}\bar{z}$, with the shear rate $\dot{\gamma} = \partial_{\bar{z}} v_x|_0 = h|\Delta P|/2\eta L$ and $\partial_{\bar{z}}$ denoting partial differentiation with respect to $\bar{z}$. The inset in Fig. 1(c) shows the shear rate values extracted from the velocity profiles for several pressure drops. As highlighted by the dashed black line, the shear rate increases linearly with the pressure drop. The slope, given by $h/2\eta L$, provides a water viscosity $\eta = 0.9 \pm 0.1$ mPa s at 24 C in agreement with the expected value [44]. In the SI, we show that $\partial_{|\Delta P|}\dot{\gamma}$ is in quantitative agreement with bulk rheological measurements of the viscosity for all of the liquids investigated here.

Having discussed the mean velocity of the particles, we turn our attention to the displacement distributions. Figures 2(a) and (b) show the probability density functions (PDFs, here called $\mathcal{P}$) of the transverse (Δy) and streamwise (Δx) displacements for 100 nm-radius particles in water over a duration $\tau = 2.5$ ms and several pressure drops. For Fig. 2 and in the following, we systematically take $z = z(t)$, the altitude at the initial observation time. This $z(t)$ should be distinguished from the average $\bar{z}$ over the lag time τ. In Fig. 2(a) it is shown that the transverse displacement PDFs do not depend on the pressure drop and are well described by a Gaussian over two decades. The global standard deviation provides an approximation for the unidimensional Brownian

diffusion coefficient $\sigma_{\Delta y}^2/2\tau \approx 2.0 \pm 0.3\ \mu$m^2 s^{-1}. Despite the lubrication effect discussed below, this estimate is close to the value predicted by the Stokes-Einstein relation $D_0 = k_{\mathrm{B}}T/6\pi\eta a \approx 2.2 \pm 0.2\ \mu$m^2 s^{-1} [45] for particles with $a = 100$ nm advected in water, where k_{B} is Boltzmann's constant and T is the temperature and η was taken from bulk rheology. Contrasting with the transverse displacement PDFs, those for the streamwise direction in Fig. 2(b) are not Gaussian, become broadened with the pressure drop, and exhibit asymmetry as seen in Ref. [33].

The TIRFM setup provides the particle distance from the glass/liquid interface through the detected intensity, allowing to distinguish the contributions of particles at different altitudes to the global PDFs. In the transverse direction, the local PDFs are shown for the largest pressure drop in Fig. 2(c) and they are all Gaussian regardless of z. In Fig. 2(d) are shown similar decompositions for the smallest and largest pressure drops for streamwise displacements. These decompositions demonstrate that the asymmetry of the global distributions is mainly due to the superposition of different mean displacements at different altitudes. For the smallest pressure drop (yellow) the local PFDs are only slightly shifted with increasing z due to the relatively low mean velocities, $cf.$ Fig. 1(c). For the largest pressure drop (red), the mean values are shifted more strongly with increasing z as a result of the higher shear rate. More importantly, the local PDFs thus provide access to the transverse diffusion along y and streamwise dispersion along x for different altitudes.

A detailed study of the local Taylor dispersion as function of time and the various physical parameters at stake is now described. In Figs. 3(a) and (b) are shown the local transverse diffusion coefficient, $D_y(z,\tau) = \sigma_{\Delta y(z)}^2/2\tau$, and the streamwise dispersion coefficient, $\mathcal{D}_x(z,\tau) = \sigma_{\Delta x(z)}^2/2\tau$. The latter comprises pure diffusive and advection effects, and is remarkably larger (up to an order of magnitude) than the former. These data were obtained from altitude decompositions as in Fig. 2 for several τ (red to blue). Figures 3(a) and (b) show that there is a general increase with z of D_y and $\mathcal{D}_x$ until reaching a plateau at large z; in the SI, we show that these plateau values are in quantitative agreement with the Stokes-Einstein relation for all liquids investigated after comparing to independently measured bulk viscosities. The variation with z in both directions is due to hydrodynamic interactions between particles and the solid/liquid interface, leading to a hindered diffusion as discussed in detail elsewhere [40, 46–48]. The z-dependence of D_y is in agreement with the prediction resulting from the effective viscosity near a flat, rigid wall [46] (see the plain black line in Fig. 3(a)). As expected, the transverse diffusion is not dependent on the lag time τ; in contrast, the dispersion coefficients increase significantly with τ as
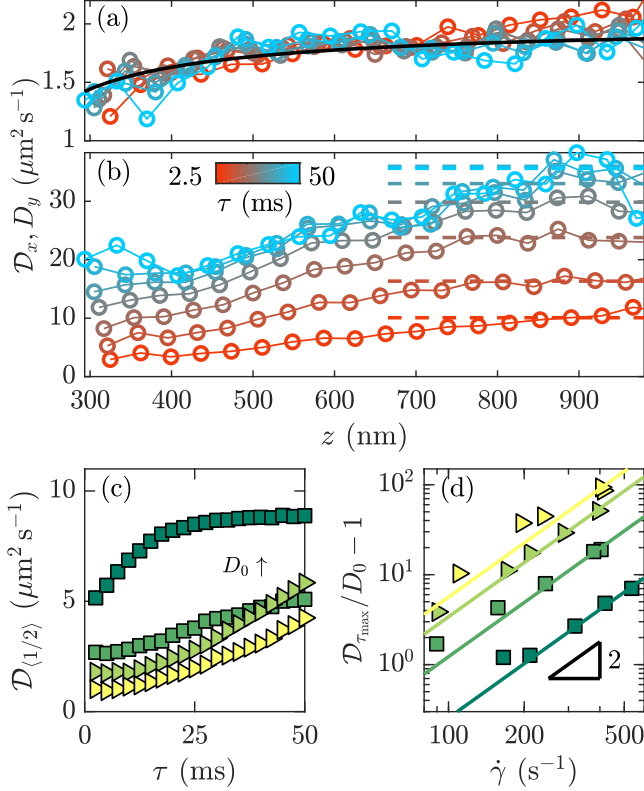
Figure 3: (a) Transverse diffusion coefficients, D_y, and (b) streamwise dispersion coefficient, $\mathcal{D}_x$, as a function the apparent altitude and lag time, τ, for 100 nm-radius particles with a pressure drop of 50 mbar across the microfluidic device. In (a), the plain black line corresponds to the theoretical prediction $D_y = D_0\left(1 - (9/16)\,Z^{-1} + (3/8)\,Z^{-3} - (45/256)\,Z^{-4} - (1/16)\,Z^{-5}\right)$ with $Z = z/a$ [46]. In (b) the dashed lines indicate the streamwise dispersion coefficient, $\mathcal{D}_{\langle 1/2\rangle}$ shown in (c) as a function of lag time. From yellow to dark green, the bulk diffusion coefficient increases. In particular —from bottom to top— the shear rates, particle radii and viscosities are $\{\dot{\gamma}, a, \eta\} = \{110, 100, 7.6\}$, $\{91, 100, 2.1\}$, $\{90, 100, 1\}$, $\{165, 55, 1\}$ in units $\{s^{-1}, \text{nm}, \text{mPa\,s}\}$; giving $D_0 = \{0.28, 0.89, 2.1, 3.9\}\,\mu m^2\,s^{-1}$ determined from the Stokes-Einstein relation. (d) Reduced late-time dispersion coefficient versus the squared shear rate; the solid lines have log-log slope 2.

shown in Fig. 3(b).

In Fig. 3(c) we show the lag-time dependence of the streamwise dispersion coefficient. To do so, we define $\mathcal{D}_{\langle 1/2\rangle}(\tau)$ as the averaged $\mathcal{D}_x(z(t),\tau)$ for all $z(t) > H/2$, where the length scale, H, is the size of the observation zone. That is, particles beginning their trajectory in the top half of the observation zone, thus limiting the aforementioned lubrication effects. In this figure, the bulk diffusion coefficient D_0 was varied by changing the particle size and the liquid viscosity. For the lowest values of D_0, $\mathcal{D}_{\langle 1/2\rangle}$ continuously increases with time and the temporal slope increases; by contrast, $\mathcal{D}_{\langle 1/2\rangle}$ saturates to a plateau for the largest D_0. As explained

by Taylor [1], the time needed to reach the dispersion plateau corresponds roughly to the time needed to diffuse across the channel height. Here the Taylor time is taken as $\tau_z = H^2/D_0$. In a rectangular channel, the exact calculation (see SI) gives a characteristic diffusion time τ_z/π^2. For the 55 nm-radius particles in water, assuming a length scale $H \approx 700$ nm, $\tau_z/\pi^2 \approx 13$ ms, in reasonable agreement with the corresponding data of Fig. 3(c), with $D_0 = 3.9 \pm 0.4\ \mu m^2\,s^{-1}$. For smaller values of D_0, the dispersion remains mainly in the short-time, increasing-slope regime. Nevertheless, taking the longest-time data available (the data of Fig. 3(c) at $\tau = 50$ ms, denoted $\mathcal{D}_{\tau_{\max}}$) for each D_0 value, we next examine the shear-rate dependence of the dispersion.

In Fig. 3(d) is shown the dependence of the reduced late-time dispersion coefficient, $\mathcal{D}_{\tau_{\max}}/D_0 - 1$, for four D_0 as a function of the shear rate. The solid lines (with slope 2 in log-log representation) show that the reduced $\mathcal{D}_{\tau_{\max}}$ increases quadratically with the shear rate $\dot{\gamma}$ for all D_0 studied. To understand this result, we applied the classical Taylor analysis (i.e. long-time limit, see SI) to a linear shear flow in a rectangular channel, giving

$$\mathcal{D}_x = D_0\left(1 + \frac{1}{120}\frac{\dot{\gamma}^2 H^4}{D_0^2}\right) \quad \tau \gg \tau_z\,, \qquad (1)$$

for the infinite-time dispersion coefficient. Identifying $\dot{\gamma}H/2$ as the mean flow velocity in the observation zone with $0 \le z \le H$, Eq. 1 is equivalent to the usual result of Taylor, i.e. $\mathcal{D}_x = D_0(1 + \alpha Pe^2)$ [1]. In this latter expression, the Péclet number is $Pe = U(H/2)/D_0$, α is a geometry-dependent prefactor and $H/2$ replaces the tube radius of a cylindrical geometry. Equation 1 highlights the key role of velocity gradients in enhanced dispersion, and justifies the linearity of the data in Fig. 3(d) for the 55 nm-radius particles in water. Applying Eq. 1 to this latter data, we extract a length scale $H \approx 500$ nm, consistent with the range of z observed in Fig. 1(c). Because the larger-D_0 data does not reach the infinite-time plateau, the prefactor for the linear regressions does not reveal the corresponding size of the flow region H. However, as we show in the following, the quadratic shear rate dependence is preserved for all time regimes, explaining the scaling of the data in Fig. 3(d).

We now examine the detailed time dependence of dispersion coefficient for all of the experimentally accessed times. Partly inspired by the shear-rate dependence of Fig. 3(d), we show in Fig. 4(a) the reduced $\mathcal{D}_{\langle 1/2\rangle}$ normalised by $(\tau_z\dot{\gamma})^2$ as a function of the dimensionless lag time, τ/τ_z. Remarkably, the data in Fig. 3(c), along with that for experiments implementing four other shear rates per D_0, collapse onto a single master curve. Such a collapse suggests the existence of a universal function describing the reduced dispersion coefficient. While in Figs. 3(c),(d) and Fig. 4(a), we consider particles beginning their trajectories in the top half of the channel, this fraction can be generalised, with n representing the frac-
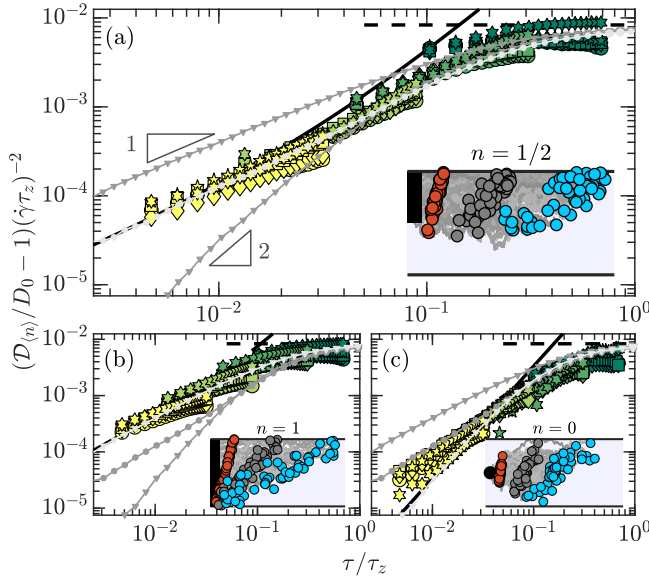
Figure 4: Reduced dispersion coefficient as a function of dimensionless time for all shear rates and D_0 studied for fractions (a) $n = 1/2$, (b) $n = 1$, and (c) $n \to 0$ of the observation zone. The bulk diffusion coefficients, D_0, for the data from dark green to yellow points are identical to those in Figs. 3(c) and (d). The black dashed and solid lines respectively correspond to the asymptotic behaviours for the long- and short-time regimes predicted by Eqs. 1 and 3. The gray lines decorated with circles and triangles correspond to the results from Langevin simulations for the $n = 1/2$, $n = 1$ and $n = 0$ conditions. For each panel, the corresponding simulation results are highlighted in lighter gray. The insets schematically show three instants of particle trajectories advected from the associated observation zone in a linear shear flow and with diffusion in z. The slope triangles in (a) denote power-law exponents 1 and 2.

tion of the observation zone from which particles leave, with $0 \le n \le 1$. The reduced dispersion is thus expected to follow a relation of the form

$$\left(\frac{\mathcal{D}_{\langle n \rangle}}{D_0} - 1\right)(\dot{\gamma}\tau_z)^{-2} = \mathcal{F}_{\langle n \rangle}\left(\frac{\tau}{\tau_z}\right) . \qquad (2)$$

Examining Fig. 4(a), we note that the reduced $\mathcal{D}_{\langle 1/2 \rangle}$ increases with time and then reaches a plateau. According to Eq. 1, in the $\tau/\tau_z \to \infty$ limit, $\mathcal{F}_{\langle n \rangle}$ is expected to reach $1/120$. This value is shown with the horizontal black dashed line and is in quantitative agreement with the data which crosses over when $\tau/\tau_z \approx 1$.

Concerning the data at the shortest dimensionless lag times in Fig. 4(a), we find that they do not follow the typically predicted [9–13] and measured [14–16] early-time τ^2 dependence. A key foundation of this τ^2 dependence is the assumption that each particle begins its trajectory at the same initial altitude. In general, however, particles may leave from a non-peaked distribution of initial altitudes. This distribution is particularly relevant for Fig. 4(a), since the plotted quantity is related to an aver-

age of all the particles in the top half of the observation zone (indicated by the dashed lines in Fig. 3(b)).

To investigate the effect of such a distribution of initial particle altitudes, we proceed by assuming that particles are 'released' at time t and position z_0 from a general distribution $\mathcal{P}_0(z_0)$ in an infinitely extended shear flow. This description should thus be valid for early times only. Given such a distribution of initial altitudes, the linear shear flow, and diffusion along the z-direction, we analytically demonstrate that Eq. 2 is the appropriate form for the lag-time-dependent, reduced short-time dispersion coefficient (see SI). In the simple case for which particles are uniformly released over a fraction n of the channel height, the function $\mathcal{F}_{\langle n \rangle}$ becomes:

$$\mathcal{F}_{\langle n \rangle}\left(\frac{\tau}{\tau_z}\right) = \frac{n^2}{24}\left(\frac{\tau}{\tau_z}\right) + \frac{1}{3}\left(\frac{\tau}{\tau_z}\right)^2, \quad \tau \ll \tau_z . \qquad (3)$$

The more general case of a non-uniform initial distribution of altitudes is also captured by our model. In that case, the prefactor of the linear term in τ/τ_z on the right-hand-side of Eq. 3 is replaced with the initial variance of the distribution normalized by the mean-square displacement in the vertical direction over the Taylor time:

$$\frac{n^2}{24} \to \frac{\langle z_0^2 \rangle - \langle z_0 \rangle^2}{2D_0\tau_z} . \qquad (4)$$

We now examine the limits of Eqs. 3 and 4. A null variance of the initial distribution arises if all particles start at the same altitude (here called the "dot" condition). For this dot condition, the classical τ^2 dependence for the reduced short-time dispersion coefficient is recovered, reflecting a steadily increasing diversity of newly sampled velocities (see SI Videos 3 and 4). The dot condition corresponds to single-particle tracking in a linear shear flow, as considered before [9–16]. For non-vanishing initial variance, the reduced dispersion coefficient has a linear temporal evolution at times shorter than the crossover time $\tau_C = 3(\langle z_0^2 \rangle - \langle z_0 \rangle^2)/2D_0$ obtained by setting the linear and quadratic terms of Eq. 3 to be equal. This linear behaviour for extended distributions results from particles at different altitudes transported different distances by the linear shear flow (SI Videos 3 and 4). When the initial variance is small with respect to H^2, a crossover into the quadratic lag-time dependence occurs, before the Taylor plateau for the observation zone is reached.

In Fig. 4(a), we consider particles leaving from the upper half of the observation zone, as schematically shown in the inset. The corresponding analytical prediction of Eqs. 2 and 3 with $n = 1/2$ is also shown in Fig. 4(a) as a black solid line. At early times, the prediction of the analytical model is in good agreement with the experimental data choosing the observation zone to be that which comprises 90 % of our particle observations.

To understand the complete time dependence including the long-time Taylor saturation, we performed numerical integrations of the overdamped Langevin equations used in [35, 49]. Here we assumed an effective channel with reflecting boundary conditions at both walls and a linear shear flow between them. For the case $n = 1/2$ (called the "half-line" condition), the reduced dispersion coefficients from these simulations are shown in Fig. 4(a) in light gray. The predictions from the Langevin equations show a complete, quantitative agreement with the experimental data with no fitting parameter. For comparison, we have also simulated cases with $n = 0$ (dot) and $n = 1$ (called the "line" condition), which at early times are well outside the experimental data limits. Furthermore, we observe that the half-line simulation is parallel to the line-condition simulation at the earliest times, and joins the simulation results for the dot and line conditions at later times. These observations are consistent with the main features of the analytical model described above (i.e. the linear-to-quadratic crossover). While the analytical model and the simulation ignore electrostatic and hydrodynamic interactions with the wall, in the SI we show that these phenomena respectively reduce the size of the effective channel but do not affect the main features of time-dependent advection-diffusion coupling discussed here.

In order to test our analytical model, we again leverage the depth resolution of the TIRFM method to select different initial distributions. First, we choose the line condition illustrated in the inset of Fig. 4(b). We thus study the dispersion coefficients for all observed particles, meaning that we consider the global distributions of Fig. 2(b). The reduced dispersions measured for this condition are shown in Fig. 4(b). The results are once again in quantitative agreement with the early-time, analytical prediction and the full-time Langevin simulations. Similarly, we consider particles leaving from a narrow altitude range, approaching the dot condition (inset of Fig. 4(c)). In Fig. 4(c) is shown the corresponding temporal evolution of the reduced dispersion coefficient for $z_0 = 600 \pm 15$ nm. While the data does not reach exactly (especially at early times) the theoretical prediction for the dot condition due to the polydispersity of the particles (and thus non-unique altitudes for a given intensity [43]), it is systematically below the one for the half-line condition and approaches the τ^2 asymptotic behaviour predicted by Eq. 3 for $n = 0$. The experimental data also agrees well with the corresponding Langevin simulation results. The data analysis and numerical simulations carried out for three different initial particle distributions using the same measurement data clearly demonstrate the crucial role of such a distribution for the short-time dispersion. Furthermore, these results validate our novel analytical model, that can be used to quantitatively rationalise general short-time dispersion observations.

To conclude, we report on an experimental, theoretical, and numerical study of advection-enhanced dispersion from short to long times compared to the classical Taylor time. We provide a quantative description of the short- and long-time dispersion behaviours. First, we show that the two regimes share the same shear-rate dependence, the shear rate being particularly large for near-surface transport where the advection-diffusion coupling should be the largest. Furthermore, we reveal and characterize how the initial particle distribution affects the short-time dispersion. Specifically, we observe a short-time, mixed-power-law behaviour for the general case, before a crossover to the well-known long-time saturation regime for linear shear flows. In the extremal cases of i) full-channel observations, a linear approach of the dispersion coefficient to the long-time value is observed, while ii) for fine depth resolutions a quadratic tendency is approached. Altogether, the experimental data are in quantitative agreement with the analytical predictions and results from Langevin numerical simulations. In the rich context of particle transport, such concepts should prove pertinent in quantitative prediction and observation of time-dependent, near-surface nanoparticle and solute dispersion, with applications related to microscopic biology and nanoscale technologies.

METHODS

All the experiments performed here employed pressure-driven flows (Fluigent MFCS-4C pressure controller) in microchannels with a rectangular section (height $h = 18$ μm, width $w = 180$ μm, length $\ell = 8.8$ cm). Microfluidic chips were fabricated by soft lithography of poly(dimethyl siloxane) (Dow Chemical, Sylgard 184) on a plasma-cleaned glass coverslip with 145 μm thickness constituting the bottom surface. The liquids used were ultra-pure water (18.2 MΩ cm, MilliQ) and water-glycerol mixtures that gave Newtonian fluids with Newtonian viscosities of $\eta = 1, 2.1$ and 7.6 mPa s, measured with a Couette-cell rheometer (Anton Paar MCR 302) up to $\dot{\gamma} = 1000$ s^{-1}. The fluorescent nanoparticles used were 55 nm-radius (Invitrogen F8803, Thermofisher) and 100 nm-radius (Invitrogen F8888 Thermofisher) latex microspheres used without further modification besides dilution by a factor of 10^3 using utra-pure water.

TIRFM measurements were realised by illuminating the near-surface shear flow with a laser source (Coherent Sapphire, wavelength $\lambda = 488$ nm, power 150 mW) focused off the central axis of, and on the back focal plane of a $100\times$ microscope objective with a large numerical aperture (NA = 1.46, Leica HCX PL APO). Large NA is required to reach incident angles θ larger than the critical angle, $\theta_c = \arcsin(n_l/n_g)$, enabling total reflection at the glass/liquid interface. Here, $n_g = 1.518$ is the refractive index of the glass coverslip, n_f is the refractive index of

the liquid and θ the angle of incidence of the laser; the refractive indices of the three liquids were measured using a refractometer (Atago PAL-RI).

The complete setup and alignment procedure are described in [50]. In the TIRFM configuration, the evanescent wave has an intensity decaying exponentially as $I(z) = I_0 \exp(-z/\Pi)$ with the penetration depth $\Pi = (\lambda/4\pi)\left(n_{\mathrm{g}}^2 \sin^2 \theta - n_{\mathrm{f}}^2\right)^{-1/2}$. Typical values of the penetration depth were thus $\Pi \approx 100$ nm, allowing for an observation of particles roughly within the first micrometer from the glass/liquid interface whereas the channel height is $h = 18$ μm. The images of 528×512 pixels (px), with 22.9 px/μm, are recorded in 16-bit format (Andor Neo sCMOS) with a frame rate of 400 Hz for a duration of 5 s. For each set of parameters (particle radius, viscosity and pressure drop), five videos of 2000 frames were recorded. Fig. 1(b) shows a superposition of 18 frames showing a single 55 nm-radius particle's near-surface trajectory in a water flow with an imposed pressure drop of 30 mbar across the microfluidic device. After a centroid detection, the intensity profile was fitted by a radially-symmetric Gaussian model for each frame. Thus the x and y coordinates give the particle position in the plane parallel to the glass/water interface whereas the particle height, z, is encoded in the intensity thanks to the exponential decay of the evanescent wave. The apparent altitude is $z = \Pi \log(I_0/I)$ [35, 43]. A discussion linked to the limitations of using this apparent altitude appears in the SI.

[1] G. I. Taylor, Proceedings of the Royal Society of London. Series A. Mathematical and Physical Sciences **219**, 186 (1953).

[2] R. Aris, Proceedings of the Royal Society of London. Series A. Mathematical and Physical Sciences **235**, 67 (1956).

[3] H. Brenner and D. Edwards, *Macrotransport Processes, edited by Butterworth* (Heinemann, 1993).

[4] H. A. Stone and H. Brenner, Industrial & Engineering Chemistry Research **38**, 851 (1999).

[5] R. R. Biswas and P. N. Sen, Physical Review Letters **98**, 164501 (2007).

[6] I. Griffiths and H. A. Stone, EPL (Europhysics Letters) **97**, 58005 (2012).

[7] M. S. Bello, R. Rezzonico, and P. G. Righetti, Science **266**, 773 (1994).

[8] C. L. Hansen, M. O. Sommer, and S. R. Quake, Proceedings of the National Academy of Sciences **101**, 14431 (2004).

[9] T. Van de Ven, Journal of Colloid and Interface Science **62**, 352 (1977).

[10] G. Batchelor, Journal of Fluid Mechanics **95**, 369 (1979).

[11] R. Foister and T. Van De Ven, Journal of Fluid Mechanics **96**, 105 (1980).

[12] C. Van den Broeck, J. Sancho, and M. San Miguel, Physica A: Statistical Mechanics and its Applications **116**, 448 (1982).

[13] K. Miyazaki and D. Bedeaux, Physica A: Statistical Mechanics and its Applications **217**, 53 (1995).

[14] H. Orihara and Y. Takikawa, Physical Review E **84**, 061120 (2011).

[15] E. O. Fridjonsson, J. D. Seymour, and S. L. Codd, Physical Review E **90**, 010301 (2014).

[16] Y. Takikawa, T. Nunokawa, Y. Sasaki, M. Iwata, and H. Orihara, Physical Review E **100**, 022102 (2019).

[17] F. Gentile, M. Ferrari, and P. Decuzzi, Annals of Biomedical Engineering **36**, 254 (2008).

[18] J. Tan, A. Thomas, and Y. Liu, Soft Matter **8**, 1934 (2012).

[19] T. K. Nielsen, U. Bösenberg, R. Gosalawit, M. Dornheim, Y. Cerenius, F. Besenbacher, and T. R. Jensen, ACS Nano **4**, 3903 (2010).

[20] A. B. Grommet, M. Feller, and R. Klajn, Nature Nanotechnology **15**, 256 (2020).

[21] J. J. Fredberg, Journal of Applied Physiology **49**, 232 (1980).

[22] J. Grotberg, Annual Review of Fluid Mechanics **26**, 529 (1994).

[23] L. Salerno, G. Cardillo, and C. Camporeale, Physical Review Fluids **5** (2020).

[24] D. Stein, F. H. van der Heyden, W. J. Koopmans, and C. Dekker, Proceedings of the National Academy of Sciences **103**, 15853 (2006).

[25] R. Bearon and A. Hazel, Journal of Fluid Mechanics **771** (2015).

[26] S. Marbach, K. Alim, N. Andrew, A. Pringle, and M. P. Brenner, Physical Review Letters **117**, 178103 (2016).

[27] S. Marbach and K. Alim, Physical Review Fluids **4**, 114202 (2019).

[28] A. Dehkharghani, N. Waisbord, J. Dunkel, and J. S. Guasto, Proceedings of the National Academy of Sciences **116**, 11119 (2019).

[29] D. Axelrod, The Journal of cell biology **89**, 141 (1981).

[30] K. N. Fish, Current Protocols in Cytometry **50**, 12 (2009).

[31] D. C. Prieve, Advances in Colloid and Interface Science **82**, 93 (1999).

[32] R. Pit, H. Hervet, and L. Léger, Physical Review Letters **85**, 980 (2000).

[33] S. Jin, P. Huang, J. Park, J. Yoo, and K. Breuer, Experiments in Fluids **37**, 825 (2004).

[34] M. Yoda and Y. Kazoe, Physics of Fluids **23**, 111301 (2011).

[35] Z. Li, L. D'eramo, C. Lee, F. Monti, M. Yonger, P. Tabeling, B. Chollet, B. Bresson, and Y. Tran, Journal of Fluid Mechanics **766**, 147 (2015).

[36] M. Yoda, Annual Review of Fluid Mechanics **52**, 369 (2020).

[37] P. Huang, J. S. Guasto, and K. S. Breuer, Journal of Fluid Mechanics **566**, 447 (2006).

[38] D. Lasne, A. Maali, Y. Amarouchene, L. Cognet, B. Lounis, and H. Kellay, Physical Review Letters **100**, 214502 (2008).

[39] C. Bouzigues, P. Tabeling, and L. Bocquet, Physical Review Letters **101**, 114503 (2008).

[40] P. Huang and K. S. Breuer, Physical Review E **76**, 046307 (2007).

[41] B. Derjaguin, Transactions of the Faraday Society **35**, 203 (1940).

[42] E. J. W. Verwey, The Journal of Physical Chemistry **51**, 631 (1947).

[43] X. Zheng, F. Shi, and Z. Silber-Li, Microfluidics and Nanofluidics **22**, 127 (2018).

[44] L. Korson, W. Drost-Hansen, and F. J. Millero, The Journal of Physical Chemistry **73**, 34 (1969).

[45] A. Einstein, Annalen der Physik **322**, 549 (1905).

[46] H. Brenner, Chemical engineering science **16**, 242 (1961).

[47] L. P. Faucheux and A. J. Libchaber, Physical Review E **49**, 5158 (1994).

[48] A. Saugey, L. Joly, C. Ybert, J.-L. Barrat, and L. Bocquet, Journal of Physics: Condensed Matter **17**, S4075 (2005).

[49] D. L. Ermak and J. A. McCammon, The Journal of Chemical Physics **69**, 1352 (1978).

[50] M. T. Hoffman, J. Sheung, and P. R. Selvin, in *Single Molecule Enzymology* (Springer, 2011), pp. 33–56.

Supplementary Information for:

Time dependence of advection-diffusion coupling for nanoparticle ensembles

Alexandre Vilquin, Vincent Bertin, Pierre Soulard, Gabriel Guyard,
Elie Raphaël, Frédéric Restagno, Thomas Salez and Joshua D. McGraw

Supplementary document information

- Video 1: Image sequences of raw experimental data for 55 nm-radius fluorescent particles advected in a pressure driven flow of pure water along a microchannel with geometry described in the text, and with an incident 488 nm-laser angle of 64 °. The videos were taken with pressure drops imposed as noted, and each frame has a width of 23 μm.

- Video 2: Identical to Video 1 but with particle trajectories superimposed.

- Video 3: Animations of particle trajectories obtained from Langevin simulations imposing 'dot', 'half-line' and 'line' initial conditions (indicated by the black regions, see main text for definitions), with diffusion along the vertical and shear flow advection along the horizontal. The animation is displayed during a dimensionless time range $0 \leq \tau/\tau_z \leq 0.1$ in the lab frame.

- Video 4: [Left] Identical to Video 3, but in the reference frame of the center of mass for the fluid and for a dimensionless time range $0 \leq \tau/\tau_z \leq 10$. The horizontal black-outlined bar in the middle panel indicates the entire observation zone at $\tau/\tau_z = 10$, and the observed region at a given instant is highlighted in red. [Right] For the three different conditions of the right panels, progression of the reduced dispersion coefficient.

- *TaylorDispersion.html*: Python/Jupyter notebook describing the overdamped Langevin simulations of Section 7, in particular reproducing Figs. S3 and S4.

1 Notations used in the main text

Coordinates

x	streamwise coordinate, direction of flow
y	transverse coordinate, flow-invariant
z	wall-normal coordinate

Times

t	particle observation time
τ	lag time
τ_z	channel exploration time
τ_C	early-time 'line-dot' crossover time

Diffusion coefficients and dispersions

D_0	bulk isotropic diffusion coefficient
D_y	diffusion coefficient in flow-invariant direction
$\mathcal{D}_x$	dispersion coefficient in the flow direction
$\mathcal{D}_{\langle n \rangle}$	dispersion coefficient in the flow direction averaged over a fraction, n of H
$\mathcal{D}_{\tau_{\max}}$	$\mathcal{D}_{\langle 1/2 \rangle}$ at late experimental times
$\mathcal{F}_{\langle n \rangle}$	reduced dimensionless analogue of $\mathcal{D}_{\langle n \rangle}$

Statistical quantities

$\mathcal{P}$	probability distribution functions
$\langle z_0 \rangle$	first moment of $\mathcal{P}_0(z_0)$
$\langle z_0^2 \rangle$	second moment of $\mathcal{P}_0(z_0)$
$\sigma_{[]}$	standard deviation of quantity $[]$

Experimental parameters

a	particle radius
η	fluid viscosity
ρ	fluid density
h	channel height
w	channel width
ℓ	channel length
H	observation domain size
n	fraction of observed flow domain
ΔP	pressure drop across channel length
v_x	flow speed along the x-direction
$\dot{\gamma}$	near-wall shear rate
U	average flow speed in Poiseuille flow
Re	Reynolds number
Pe	Péclet number
α	Taylor's geometric dispersion factor
λ	illumination laser wavelength
n_f	index of refraction: fluid
n_g	index of refraction: glass substrate
θ	incident laser angle
θ_c	critical incident angle
Π	evanescent wave penetration length
I	particle fluorescence intensity
I_0	particle fluorescence intensity at the solid/liquid interface

2 Intensity distribution and mean velocity profiles

This section provides additional information about how the observed signal intensity distributions (SIDs after Zheng and coworkers [1], denoted $\mathcal{P}_{\mathrm{SID}}$) and the corresponding velocity profiles can be quantitatively described simultaneously. As also described by Li and coworkers [2], fluorescent nanoparticles detected have a limited range of intensities affected by several factors, the most important ones being, and as discussed in turn: i) electrostatic interactions which determine the probability that a particle of a given radius is found at a certain distance from the wall according to a Boltzmann distribution; ii) particle size distribution; and iii) the optical setup which, given the position and size of the particle, finally determines its intensity. We now discuss each of these elements in detail.

$-i-$ The glass surface exerts an electrostatic repulsion on the particles according to the fact that both surfaces are negatively charged; the details of such a repulsion are understood within the Derjaguin-Landau-Verwey-Overbeek (DLVO) framework [3, 4]. This electrostatic interaction potential, ϕ_{el}, describing the electric double-layer repulsion between a particle with radius R and a flat wall [5] is given by:

$$\phi_{\mathrm{el}}\left(z_{\mathrm{c}}\right) = 16\epsilon R\left(\frac{k_{\mathrm{B}}T}{e}\right)^2 \tanh\left(\frac{e\psi_{\mathrm{p}}}{4k_{\mathrm{B}}T}\right) \tanh\left(\frac{e\psi_{\mathrm{w}}}{4k_{\mathrm{B}}T}\right) \exp\left(-\frac{z_{\mathrm{c}}-R}{l_{\mathrm{D}}}\right). \qquad (\mathrm{S1})$$

Here, z_{c}, ϵ, e, ψ_{p}, ψ_{w} and l_{D} are respectively the position of the center of the particle, liquid permittivity, elementary charge, particle and wall electrostatic potentials and the Debye length. This interaction determines the particle concentration C at thermal equilibrium through the Boltzmann distribution

$$C(z_{\mathrm{c}}) \propto \exp\left(-\frac{\phi_{\mathrm{el}}\left(z_{\mathrm{c}}\right)}{k_{\mathrm{B}}T}\right) . \qquad (\mathrm{S2})$$

As already observed in TIRFM experiments, the van der Waals interaction can be neglected for pure water [1, 2]. Consequently, the typical distance between the bottom surface (located at $z = 0$) and the particles is mainly determined by the Debye length.

$-ii-$ All the particles do not have the same radius R. The radius distribution is usually described by a Gaussian probability function

$$\mathcal{P}_R\left(R\right) = \frac{1}{\sqrt{2\pi\sigma_R^2}} \exp\left(-\frac{(R-a)^2}{2\sigma_R^2}\right) , \qquad (\mathrm{S3})$$

where a is the mean radius and σ_R its standard deviation.

$-iii-$ The fluorescence intensity, I, of an individual particle is determined by the optical parameters of the TIRFM setup and the particle's size, with $I \propto R^3$. The evanescent wave has a penetration depth Π characterizing the exponential decrease of excitation. The observed fluorescence intensity is also sensitive to the finite depth of field, d_{f}, of the microscope objective. In our experiments, the depth of field has a value of 415 nm, meaning that if particles are not located on the focal plane at z_{f} (typically 400-500 nm from the glass-liquid interface), they will be detected with a relatively low intensity. Putting these elements together, the observed fluorescence intensity for an individual particle is predicted [1] as

$$\frac{I\left(R, z_{\mathrm{c}}\right)}{I_0} = \left(\frac{R}{a}\right)^3 \exp\left(-\frac{z_{\mathrm{c}}-R}{\Pi}\right) \left[1 + \left(\frac{z_{\mathrm{c}}-R-z_{\mathrm{f}}}{d_{\mathrm{f}}}\right)^2\right]^{-1} , \qquad (\mathrm{S4})$$

where I_0 is the intensity for a particle with radius $R = a$ located at the bottom surface $z_{\mathrm{c}} = a$ and with the focal plane at the wall ($z_{\mathrm{f}} = 0$).

Using a home-made MATLAB interface, we combine Eqs. S1-S4 to generate theoretical SIDs numerically. Practically, we determine the fraction of particles having an altitude z_{c}
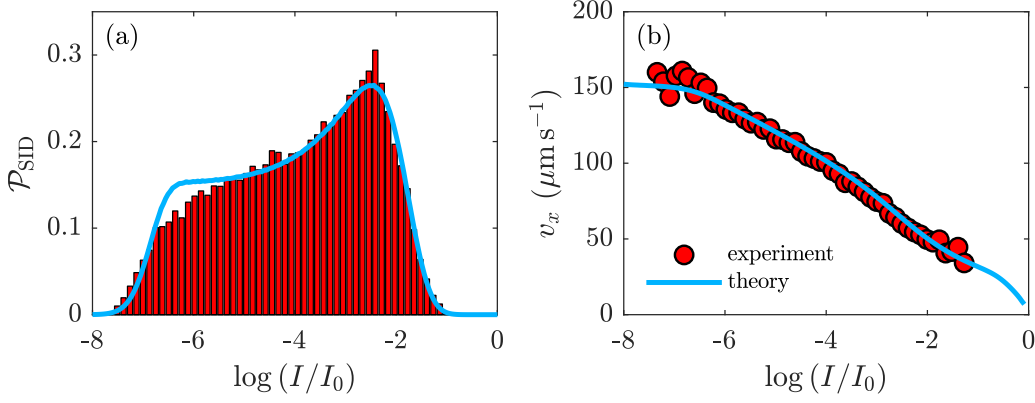
Figure S1: *(a) Comparison between experimental and theoretical signal intensity distributions (SIDs). (b) Comparison between experimental and theoretical streamwise mean velocity profiles. The experimental data is for 55 nm-radius particles for a pressure drop of 30 mbar across the microchannel.*

and a radius R given by the weight $W(z_c, R) = C(z_c)\mathcal{P}_R(R)$, and compute the associated intensity given by Eq. S4. This procedure gives a list of weighted intensities forming the blue line shown in Fig. S1(a) using a DLVO prefactor $16a\epsilon(k_BT/e)^2 \tanh(e\Psi_p/4k_BT) \tanh(e\Psi_w/4k_BT) = 1.4 \times 10^{-21}$ J, $l_D = 60$ nm, $\sigma_R = 5.5$ nm, $a = 55$ nm and the optical parameters as described above, along with the experimental histogram (red).

In addition, we also quantitatively describe the mean streamwise velocity profile, which, as noted before [2], is not perfectly linear when using the apparent altitude $z = z_c - a = \Pi \ln(I_0/I)$ defined in the main article. We assume that a particle located at an altitude z_c has a mean streamwise velocity v_x given by $v_x(z) = f_B\dot{\gamma}z$, where $\dot{\gamma}$ is the shear rate and f_B the "Brenner factor" [6]. This factor provides the hydrodynamic correction induced by the finite size of the spherical particle, when the latter is advected by a linear shear flow near a wall. For large z_c/R, the Brenner factor can be expressed as $f_B \simeq 1 - (5/16)(z_c/R)^{-3}$. For 55 nm-radius particles typically located at distances larger than 200 nm due to electrostatic repulsion, the deviation from the linear velocity profile is less than 1%.

Using the proposed particle velocity profile in conjunction with the intensity-altitude-probability relations (Eqs. S1-S4), we follow Zheng *et al.* [1] and predict the particle's mean streamwise velocity as a function of $\log(I_0/I)$. Such a prediction is made with $\dot{\gamma}$ adjusted simultaneously to the physical and optical parameters of Eqs. S1-S4. The result is shown together with the experimental results in Fig. S1(b), showing good agreement and capturing the main nonlinear features of the experimental data. The shear-rate values obtained with this SID method are approximately 15% smaller than the ones directly obtained using a linear regression of the velocity profiles of Fig. 1(c) using the apparent altitude. This discrepancy is mainly due to the particle polydispersity and to the finite depth of field of the microscope objective, and since it is only a constant factor (verified) across all experiments it does not change the main conclusions of the article.

3 Medium viscosity and particle diffusion

In Fig. 1(c), we show the streamwise velocity profiles for 55 nm-radius particles in a water flow obtained by total internal reflection fluorescence microscopy (TIRFM). In the corresponding inset, we show the associated shear rate $\dot{\gamma}$ (obtained from a linear regression on a given velocity profile) as a function of the pressure drop ΔP across the channel. Similar measurements were done for the 100 nm-radius particles in water and water-glycerol mixtures presented in the main article, see Figs. 3 and 4. Corresponding to these shear rate measurements, we can compute the stress, $\Sigma = h\Delta P/2\ell$, from the pressure
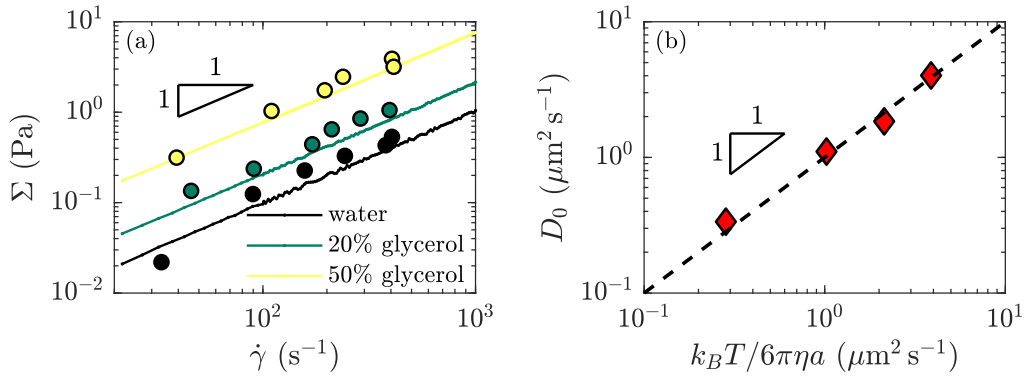
4

Figure S2: *(a) Comparison for stresses Σ versus shear rate $\dot{\gamma}$ between TIRFM (circles) and rheology measurements (lines) for 100 nm-radius particles, see inset of Fig. 1(c) for $a = 55$ nm particles in water. For TIRFM, the stress is calculated as $\Sigma = h\Delta P/2\ell$ where ΔP is the pressure gap in the channel, h and ℓ are the channel height and length. (b) Bulk diffusion coefficient D_0, measured from the plateau values of local transverse mean square displacements, versus the theoretical values calculated using the viscosity measured with a rheometer, for all particle sizes and water-glycerol mixtures. The black dashed line shows the linear relation with unit prefactor.*

drop across the rectangular channel using a geometric prefactor (height $h = 18$ μm, width $w = 180$ μm, length $\ell = 8.8$ cm). The stress Σ is plotted as a function of the shear rate $\dot{\gamma}$ in Fig. S2(a) and compared with bulk rheology measurements carried out in a Couette cell (see Methods). First, the resulting linear power laws show that all the solutions remain Newtonian for shear rates up to 1000 s^{-1}. Second, the viscosity defined as $\eta = \Sigma/\dot{\gamma}$ is consequently constant for a given solution, and it increases with the glycerol proportion. The results show a good agreement with the rheology measurements, validating both the shear rate and viscosity values obtained by TIRFM.

The viscosity values obtained further allow us to verify that the bulk diffusion coefficients measured with TIRFM are consistent with the Stokes-Einstein relation. As shown in Fig. 3(a) in the main article, the bulk diffusion coefficient D_0 is obtained from the plateau value of the local transverse diffusion coefficient D_y, calculated from the transverse mean-square displacement $\sigma^2_{\Delta y}$, through: $D_y = \sigma^2_{\Delta y}/2\tau$, where τ is the lag time. In Fig. S2(b) is shown a comparison between the experimental results and the prediction given by the Stokes-Einstein relation [7]: $D_0 = k_\text{B}T/6\pi\eta a$, after having used the independent, rheologically measured viscosity. The good agreement validates the statistical method to obtain the bulk diffusion coefficient.

4 Taylor dispersion for a linear shear flow in a channel with a rectangular section: long times

Here, we justify the expression (see Eq. 1 of the main article) of the dispersion coefficient for a linear shear flow in the long-time limit:

$$\mathcal{D}_x = D_0 \left(1 + \frac{1}{120}\frac{\dot{\gamma}^2 H^4}{D_0^2}\right), \quad \tau \gg \tau_z \ . \tag{S5}$$

The classical Taylor dispersion coefficient is typically calculated for a channel with either a circular or a rectangular section and for a Poiseuille flow [8]. To interpret the results described in Figs. 3 and 4 in the main article, we revisit its derivation for a linear shear flow. First, we consider a population of identical spherical colloids, in a rectangular channel of height H, subjected to a linear shear flow $v_x(z) = \dot{\gamma}z$ along the x-axis, where $\dot{\gamma}$ is a constant

shear rate and where $0 \leqslant z \leqslant H$. Thus, the mean velocity along x is $\frac{1}{H} \int_0^H v_x(z) \, dz = \dot{\gamma} H/2$. We assume invariance in the y-direction which is valid in the experiments. We also neglect hydrodynamic interactions with the walls, which would introduce a z-dependence of the diffusion coefficients in both the streamwise and wall-normal directions. Therefore, all the colloids are assumed to have the same, bulk diffusion coefficient D_0. The colloidal concentration field $c(x, z, t)$ evolves with time t, from both advection by the imposed flow and diffusion, as described by the advection-diffusion equation:

$$\partial_t c + v_x \partial_x c = D_0 \left(\partial_x^2 c + \partial_z^2 c \right). \tag{S6}$$

Introducing the streamwise length scale L, a concentration scale c_0, the dimensionless variables $Z = z/H$, $X = x/L$, $T = tD_0/H^2$, $C(X, Z, T) = c(x, z, t)/c_0$, $V(Z) = v_x(z)/\dot{\gamma}H$, the Péclet number $\text{Pe} = \dot{\gamma}H^2/D_0$ and the aspect ratio $\varepsilon = H/L$, Eq. (S6) becomes:

$$\partial_T C + \varepsilon \text{Pe} V(Z) \partial_X C = \varepsilon^2 \partial_X^2 C + \partial_Z^2 C. \tag{S7}$$

We decompose the concentration profile through:

$$C(X, Z, T) = \bar{C}(X, T) + C'(X, Z, T), \tag{S8}$$

with $\bar{C}(X, T) = \int_0^1 C(X, Z, T) \, dZ$ the thickness-averaged concentration and C' the deviation from the latter. Inserting this decomposition into Eq. (S7), one obtains:

$$\partial_T \bar{C} + \partial_T C' + \varepsilon \text{Pe} V(Z) \partial_X \bar{C} + \varepsilon \text{Pe} V(Z) \partial_X C' = \varepsilon^2 \partial_X^2 \bar{C} + \varepsilon^2 \partial_X^2 C' + \partial_Z^2 C'. \tag{S9}$$

Averaging further over Z leads to:

$$\partial_T \bar{C} + \varepsilon \text{Pe} \frac{1}{2} \partial_X \bar{C} + \varepsilon \text{Pe} \overline{V \partial_X C'} = \varepsilon^2 \partial_X^2 \bar{C} + \varepsilon^2 \overline{\partial_X^2 C'}, \tag{S10}$$

where we assumed no normal colloidal flux at the channel boundary. Subtracting the two last equations with one another gives:

$$\partial_T C' + \varepsilon \text{Pe} \left(V - \frac{1}{2} \right) \partial_X \bar{C} + \varepsilon \text{Pe} \left(V \partial_X C' - \overline{V \partial_X C'} \right) = \varepsilon^2 \left(\partial_X^2 C' - \overline{\partial_X^2 C'} \right) + \partial_Z^2 C'. \tag{S11}$$

Invoking now the long-time condition proposed by Taylor [8], $T \gg 1$, the concentration field becomes nearly homogeneous along Z leading to $C' \ll \bar{C}$. In addition, we have $\varepsilon \ll 1$. All together, Eq. (S11) can be simplified into:

$$\partial_Z^2 C' \simeq \varepsilon \text{Pe} \left(V - \frac{1}{2} \right) \partial_X \bar{C}. \tag{S12}$$

Since the thickness-averaged concentration field $\bar{C}$ does not depend on Z, a first integration gives:

$$\partial_Z C' = \varepsilon \text{Pe} \partial_X \bar{C} \left(\frac{Z^2}{2} - \frac{Z}{2} \right) + c_1, \tag{S13}$$

where c_1 is a constant. Due to the impermeability of the channel walls, the no-flux boundary conditions are $\partial_Z C' \, |_{Z=0} = 0$ and $\partial_Z C' \, |_{Z=1} = 0$ giving $c_1 = 0$. Thus, the second integration gives:

$$C' = \varepsilon \text{Pe} \partial_X \bar{C} \left(\frac{Z^3}{6} - \frac{Z^2}{4} + c_2 \right). \tag{S14}$$

By definition, the thickness average of the deviation field C' is zero, leading to:

$$C' = \varepsilon \text{Pe} \partial_X \bar{C} \left[\frac{Z^3}{6} - \frac{Z^2}{4} + \frac{1}{24} \right]. \tag{S15}$$

Invoking the found relation between C' and $\bar{C}$, Eq. (S10) becomes:

$$\partial_T \bar{C} + \frac{1}{2}\varepsilon \mathrm{Pe}\partial_X \bar{C} = \varepsilon^2 \left(1 + B\mathrm{Pe}^2\right)\partial_X^2 \bar{C}, \tag{S16}$$

with B a dimensionless factor given by:

$$B = -\int_0^1 \mathrm{d}Z\, Z \left(\frac{Z^3}{6} - \frac{Z^2}{4} + \frac{1}{24}\right) = \frac{1}{120}. \tag{S17}$$

Putting back the dimensions and adding the definition $\bar{c} = c_0 \bar{C}$, we obtain the final equation for the long-time limit:

$$\partial_t \bar{c} + \frac{\dot{\gamma}H}{2}\partial_x \bar{c} = \mathcal{D}_x \partial_x^2 \bar{c}, \tag{S18}$$

with the dispersion coefficient $\mathcal{D}_x = D_0 \left(1 + B\mathrm{Pe}^2\right)$ where $B = 1/120$. Therefore, at long times, the thickness-averaged colloidal concentration field is advected with the mean velocity $\dot{\gamma}H/2$ and diffuses with the effective diffusion coefficient:

$$\mathcal{D}_x = D_0 \left(1 + \frac{1}{120}\frac{\dot{\gamma}^2 H^4}{D_0^2}\right), \quad \tau \gg \tau_z. \tag{S19}$$

5 Taylor time in a channel with a rectangular section

Here, we justify that the relaxation of an initial concentration profile in a rectangular channel takes place over the time scale τ_z/π^2 where the Taylor time is $\tau_z = H^2/D_0$. This quantity corresponds to the time beyond which the dispersion coefficient, Eq. (S19), calculated above becomes valid. According to Taylor [8], this time scale corresponds additionally to the duration needed to have a homogenous concentration field along z. This phenomenon is only due to the diffusion along z, leading us to solve:

$$\partial_t c = D_0 \partial_z^2 c, \tag{S20}$$

where $c(z, t)$ is the concentration field, the other spatial dependencies being irrelevant. We assume an initial concentration field $c(z, t = 0) = c_0(z)$ and solve the diffusion equation on a domain $z \in [0, H]$ along with impermeability boundary conditions: $\partial_z c(z, t) = 0$ at $z = 0$ and $z = H$. This problem can be solved exactly using the spectral decomposition:

$$c(z, t) = \bar{c} + \sum_{k=1}^{\infty} a_k(t) \cos\left(\frac{k\pi z}{H}\right), \tag{S21}$$

where $\bar{c}$ denotes the thickness-averaged concentration, and the coefficients a_k follow the linear ordinary differential equations: $\partial_t a_k = -D_0(k\pi/H)^2 a_k$. The general solution of this diffusion problem is

$$c(z, t) = \bar{c} + \sum_{k=1}^{\infty} a_{k,0} \cos\left(\frac{k\pi z}{H}\right) \exp\left(-\frac{k^2 \pi^2 D_0 t}{H^2}\right), \tag{S22}$$

where $a_{k,0} = a_k(0) = (2/H)\int_0^H c_0(z)\cos(k\pi z/H)\,\mathrm{d}z$. As a result, the slowest decaying mode $k = 1$ has a typical decay time $H^2/\pi^2 D_0 = \tau_z/\pi^2$ as desired.

6 Taylor dispersion in a linear shear flow at short times for different initial particle distributions: short times

In this section, we first provide the derivation of the short-term dispersion coefficient for a general distribution of initial particle altitudes in free space, before addressing the particular case of uniform distributions. A central assumption of the model presented in the main article is that the short-time Taylor dispersion in a channel, behaves in the same way as for an infinitely-extended medium. It is supported by the fact that the wall-normal diffusion of a particle in the channel is not affected by the presence of the walls at short times. Therefore, this assumption is valid only for time scales much shorter than the typical time $\tau_z = H^2/D_0$ for diffusion over the channel height, as introduced in the previous section.

6.1 General distribution of initial particle altitudes in free space

In this subsection, we justify how the short-time dispersion coefficient for a unique particle in a linear shear flow [9, 10, 11, 12, 13] $\mathcal{D}_x = D_0 \left(1 + \dot{\gamma}^2 \tau^2/3\right)$, is modified by considering a group of particles leaving from different altitudes z. The single-particle expression, analogous to the 'dot' condition in the main article, is neither valid in our experiments nor in the general case. Thus, we consider particles that are advected in a shear flow after having started at $x = 0$, from different initial altitudes z_0 described by the probability density function (PDF) $\mathcal{P}_0 (z_0)$. The particles are assumed to diffuse in an infinite space along z. We stress that the hydrodynamic and electrostatic interactions with the wall, which are present in the experiments, are neglected here. We will discuss their effects on the Taylor dispersion in the next section, using Langevin simulations.

The calculation of the dispersion coefficient $\mathcal{D}_x = \sigma_{\Delta x}^2/2\tau$ requires the variance $\sigma_{\Delta x}^2 = \left\langle \Delta x^2 \right\rangle - \left\langle \Delta x \right\rangle^2$ of the streamwise displacement $\Delta x (\tau) = x (t + \tau) - x (t)$. We assume here a linear shear flow, with a velocity $v_x (z) = \dot{\gamma}z$ along x. We do not consider the streamwise Brownian motion since it is not correlated to the advection and can be superimposed afterwards by linearity. Besides, the experimental time scale is much larger than the typical cross-over time between ballistic and diffusive motion (approximately 1 ns) so that we consider the overdamped dynamics. Therefore the governing equation in the streamwise direction is $\partial_t x = \dot{\gamma}z$. Upon integration, one gets:

$$\Delta x (\tau) = \dot{\gamma} \int_0^\tau \mathrm{d}t\, z (t).$$

(S23)

The mean value of the displacement is thus:

$$\left\langle \Delta x (\tau) \right\rangle = \dot{\gamma} \int_0^\tau \mathrm{d}t\, \left\langle z (t) \right\rangle.$$

(S24)

In this model, the vertical motion is purely Brownian and is described by the overdamped Langevin equation: $\partial_t z = \sqrt{2D_0}\xi (t)$, where $\xi(t)$ is a Gaussian white noise. The corresponding one-dimensional Brownian propagator is:

$$\mathrm{P}_z (z, t | z_0, t_0) = \frac{1}{\sqrt{2\pi D_0 (t - t_0)}} \exp\left[-\frac{(z - z_0)^2}{2D_0 (t - t_0)} \right].$$

(S25)

$\mathrm{P}_z (z, t | z_0, t_0)$ represents the density of probability per unit length for the particle to be located at altitude z at time t, under the condition that the particle was located at z_0 at time t_0. From P_z and Eq. (S24), one obtains $\left\langle \Delta x \right\rangle = \dot{\gamma} \left\langle z_0 \right\rangle \tau$.

Moving to the calculation of the second moment, we have the general form:

$$\left\langle \Delta x^2 \left(\tau\right) \right\rangle = \dot{\gamma}^2 \int_0^\tau \mathrm{d}t_1 \int_0^\tau \mathrm{d}t_2 \left\langle z\left(t_1\right) z\left(t_2\right) \right\rangle, \tag{S26}$$

which can be calculated from the propagator P_z. We note that the averaged quantity $\left\langle z\left(t_1\right) z\left(t_2\right) \right\rangle$ is the product of the particle altitude at time t_1 and the particle altitude at time t_2 for a *unique* trajectory, and consequently:

$$\left\langle z\left(t_1\right) z\left(t_2\right) \right\rangle \neq \int \mathrm{d}z_1 \int \mathrm{d}z_2\, z_1 \mathrm{P}_z\left(z_1, t_1 | z_0, t_0\right) z_2 \mathrm{P}_z\left(z_2, t_2 | z_0, t_0\right). \tag{S27}$$

Assuming $t_1 < t_2$, the correct expression is provided by the Markovian properties of Brownian motion and reads:

$$\left\langle z\left(t_1\right) z\left(t_2\right) \right\rangle = \int \mathrm{d}z_1 \int \mathrm{d}z_2\, z_1 \mathrm{P}_z\left(z_1, t_1 | z_0, t_0\right) z_2 \mathrm{P}_z\left(z_2, t_2 | z_1, t_1\right). \tag{S28}$$

Knowing that $\int \mathrm{d}z_2\, z_2 \mathrm{P}_z\left(z_2, t_2 | z_1, t_1\right) = z_1$ and choosing $t_0 = 0$, we have:

$$\left\langle z\left(t_1\right) z\left(t_2\right) \right\rangle = \int \mathrm{d}z_1\, z_1^2 \mathrm{P}_z\left(z_1, t_1 | z_0, t_0\right) = z_0^2 + 2D_0 t_1. \tag{S29}$$

Without the assumption $t_1 < t_2$, the latter expression is generalized as:

$$\left\langle z\left(t_1\right) z\left(t_2\right) \right\rangle = z_0^2 + 2D_0 \min\left(t_1, t_2\right), \tag{S30}$$

and we note here that $t = t_1 = t_2$ leads to the classical result $\left\langle z^2\left(t\right) \right\rangle - \left\langle z\left(t\right) \right\rangle^2 = 2D_0 t$.

In the case of an initial assembly of spatially-distributed identical particles, according to the PDF $\mathcal{P}_0\left(z_0\right)$, the latter equation is replaced by its average over z_0:

$$\left\langle z\left(t_1\right) z\left(t_2\right) \right\rangle = \left\langle z_0^2 \right\rangle + 2D_0 \min\left(t_1, t_2\right). \tag{S31}$$

By inserting this expression in Eq. (S26), one gets:

$$\left\langle \Delta x^2 \left(\tau\right) \right\rangle = \dot{\gamma}^2 \int_0^\tau \mathrm{d}t_1 \int_0^\tau \mathrm{d}t_2 \left[\left\langle z_0^2 \right\rangle + 2D_0 \min\left(t_1, t_2\right)\right]. \tag{S32}$$

Invoking the decomposition $\int_0^\tau \mathrm{d}t_2 = \int_0^{t_1} \mathrm{d}t_2 + \int_{t_1}^\tau \mathrm{d}t_2$, it follows:

$$\left\langle \Delta x^2 \left(\tau\right) \right\rangle = \dot{\gamma}^2 \left\langle z_0^2 \right\rangle \underbrace{\int_0^\tau \mathrm{d}t_1 \int_0^\tau \mathrm{d}t_2}_{\tau^2} + 2\dot{\gamma}^2 D_0 \int_0^\tau \mathrm{d}t_1 \left(\underbrace{\int_0^{t_1} \mathrm{d}t_2\, t_2}_{t_1^2/2} + \underbrace{\int_{t_1}^\tau \mathrm{d}t_2\, t_1}_{(\tau - t_1)t_1} \right), \tag{S33}$$

and thus:

$$\left\langle \Delta x^2 \left(\tau\right) \right\rangle = \dot{\gamma}^2 \left\langle z_0^2 \right\rangle \tau^2 + \frac{2}{3}\dot{\gamma}^2 D_0 \tau^3. \tag{S34}$$

From the above expressions of the average and mean-squared displacements, and adding further the independent contribution due to streamwise Brownian motion, the variance of the streamwise displacement becomes:

$$\sigma_{\Delta x}^2 \left(\tau\right) = 2D_0 \tau + \dot{\gamma}^2 \left(\left\langle z_0^2 \right\rangle - \left\langle z_0 \right\rangle^2 \right) \tau^2 + \frac{2}{3}\dot{\gamma}^2 D_0 \tau^3. \tag{S35}$$

Therefore, the dispersion coefficient can be finally expressed as:

$$\mathcal{D}_x = D_0 + \dot{\gamma}^2 \frac{\left\langle z_0^2 \right\rangle - \left\langle z_0 \right\rangle^2}{2}\tau + \frac{1}{3}\dot{\gamma}^2 D_0 \tau^2. \tag{S36}$$

9

The quadratic dependance in lag time τ predicted by the term $\dot{\gamma}^2 D_0 \tau^2/3$ is known and is in agreement with several theoretical [9, 10, 11, 12, 13] and experimental [14, 15, 16] works. The role of the different initial altitudes appears in the additional term $\dot{\gamma}^2 \left(\langle z_0^2 \rangle - \langle z_0 \rangle^2 \right) \tau/2$. This term is linear in lag time and dominates for time scales smaller than the crossover time $\tau_C = 3 \left(\langle z_0^2 \rangle - \langle z_0 \rangle^2 \right)/2D_0$, which corresponds to a typical time needed to diffuse over the standard deviation of the initial distribution $\mathcal{P}_0$ in altitudes z_0.

6.2 Application to uniform distributions of initial altitudes

We focus now on the particular case of uniform distributions of initial particle altitudes. In practice, we specify further the central term $\dot{\gamma}^2 \left(\langle z_0^2 \rangle - \langle z_0 \rangle^2 \right) \tau/2$ obtained in the previous subsection.

The simplest situation, used to obtain the classical formula $\mathcal{D}_x = D_0 \left(1 + \dot{\gamma}^2 \tau^2/3 \right)$, is to consider that all the particles leave from a unique initial altitude z_i. This corresponds to the PDF $\mathcal{P}_0 (z_0) = \delta (z_0 - z_i)$, where δ is the Dirac distribution. From the latter, it follows that $\langle z_0 \rangle^2 = \langle z_0^2 \rangle = z_i^2$, leading to the vanishing of the linear term in lag time in the dispersion coefficient.

A more general situation arises by considering that the particles are initially uniformly distributed over a vertical segment of length nH and centred at altitude z_i, where n is the dimensionless fraction of the typical vertical length H. Note that, when comparing with experimental data (see Fig. 4 in the main article), H denotes the thickness of the observation zone. This situation is described by the PDF:

$$\mathcal{P}_0 (z_0) = \begin{cases} 0 & \text{if } |z_0 - z_i| > nH/2 \\ 1/nH & \text{if } |z_0 - z_i| \leqslant nH/2 \end{cases}. \tag{S37}$$

Thus, the additional term $\dot{\gamma}^2 \left(\langle z_0^2 \rangle - \langle z_0 \rangle^2 \right) \tau/2$ due to the initial distribution of altitudes, can be calculated explicitly by expressing the average initial altitude:

$$\langle z_0 \rangle = \int_0^H \mathrm{d}z_0 \, \mathcal{P}_0 (z_0) \, z_0 = \frac{1}{nH} \int_{z_i - nH/2}^{z_i + nH/2} \mathrm{d}z_0 \, z_0 = z_i, \tag{S38}$$

and the variance in initial altitude:

$$\langle z_0^2 \rangle = \int_0^H \mathrm{d}z_0 \, \mathcal{P}_0 (z_0) \, z_0^2 = \frac{1}{nH} \int_{z_i - nH/2}^{z_i + nH/2} \mathrm{d}z_0 \, z_0^2 = z_i^2 + \frac{(nH)^2}{12}. \tag{S39}$$

Consequently, Eq. (S36) becomes:

$$\mathcal{D}_x (\tau) = D_0 + \dot{\gamma}^2 \frac{(nH)^2}{24} \tau + \frac{1}{3} \dot{\gamma}^2 D_0 \tau^2, \tag{S40}$$

where the weight of the linear term in lag time depends solely on the spatial extent of the initial distribution, but not on the average initial altitude z_i itself. Note that this bulk result is expected to be modified in presence of confinement and interfacial effects. Finally, by invoking the time scale $\tau_z = H^2/D_0$ as in the main article, we obtain the dimensionless equation:

$$\left(\frac{\mathcal{D}_x}{D_0} - 1 \right) (\dot{\gamma} \tau_z)^{-2} = \frac{n^2}{24} \frac{\tau}{\tau_z} + \frac{1}{3} \left(\frac{\tau}{\tau_z} \right)^2. \tag{S41}$$

We recall that this expression is valid for short lag times τ compared to the Taylor time τ_z/π^2. Interestingly, this single expression allows us to consider various initial uniform distributions, from the classical "dot condition" $(n = 0)$ to a complete "line condition" $(n = 1)$. As shown in the main article, this equation is in good agreement with our experiments in the short-time limit.

10

7 Simulation of Langevin equations

In this section, we provide details on the simulations of the Langevin equations, corresponding to the results shown in the main article (see Fig. 4) for comparison with our experimental results and with the analytical models described in the previous sections.

7.1 General Langevin model

For a single Brownian particle of position coordinates x_i, with i the coordinate index, advected in an external flow field characterized by the fluid velocity components v_i, the discrete overdamped Langevin equations read in the Ito convention [17]:

$$x_i\left(t+\delta t\right)=x_i\left(t\right)+v_i\delta t+\frac{D_i\left(t\right)F_i\left(t\right)}{k_{\mathrm{B}}T}\delta t+\partial_{x_i}D_i\mid_{x_i(t)}\delta t+\sqrt{2D_i\left(t\right)\delta t}\,S\left(0,1\right),\quad\text{(S42)}$$

where the diffusion coefficients D_i are non-isotropic and space-dependent in the general case, as a consequence of hydrodynamic interactions with the walls. Here, k_{B} denotes the Boltzmann constant, T the absolute temperature, $S\left(m,\sigma\right)$ a Gaussian distribution with mean value m and standard deviation σ, and F_i the components of the external force exerted on the particle.

More specifically, we consider the bidimensional problem of a Brownian particle advected along x by a linear shear flow near a wall. Gravity is neglected such that the only external force considered is the electrostatic force F_{el} exerted by the wall in the normal direction z. The fluid velocity profile is given by $v_x\left(z\right)=\dot{\gamma}z$, with $\dot{\gamma}$ a constant shear rate. Eq. (S42) thus becomes:

$$x\left(t+\delta t\right)=x\left(t\right)+\dot{\gamma}z\left(t\right)\delta t+\sqrt{2D_x(z\left(t\right))\delta t}\,S\left(0,1\right)\ ,\quad\text{(S43)}$$

$$z\left(t+\delta t\right)=z\left(t\right)+\partial_zD_z\mid_{z(t)}\delta t+\frac{D_z(z\left(t\right))F_{\mathrm{el}}(z\left(t\right))}{k_{\mathrm{B}}T}\delta t+\sqrt{2D_z(z\left(t\right))\delta t}\,S\left(0,1\right)\ .\quad\text{(S44)}$$

For a particle with a radius R, the bulk diffusion coefficient is given by $D_0=k_{\mathrm{B}}T/6\pi\eta R$, with η the dynamic shear viscosity of the liquid. We introduce the dimensionless variable $Z=z/R$. Due to the hydrodynamic interactions with the wall, the streamwise and wall-normal diffusion coefficients are modified as $D_i=D_0\beta_i$ [18, 2], with:

$$\beta_x\left(Z\right)=1-\frac{9}{16}Z^{-1}+\frac{1}{8}Z^{-3}-\frac{45}{256}Z^{-4}-\frac{1}{16}Z^{-5}+O\left(Z^{-6}\right)\ ,\quad\text{(S45)}$$

$$\beta_z\left(Z\right)=\frac{6(Z-1)^2+2(Z-1)}{6(Z-1)^2+9(Z-1)+2}\ .\quad\text{(S46)}$$

Finally, the electrostatic force is given by $F_{\mathrm{el}}=-\partial_z\phi_{\mathrm{el}}$, where ϕ_{el} is the repulsive electrostatic potential due to the double layer [1] (see section 2). In the simulations, the van der Waals interactions are neglected.

7.2 Taylor dispersion for tracer particles

We numerically integrate Eqs. (S43) and (S44) with a home-made PYTHON program, see the associated Jupyter notebook (*TaylorDispersion.html*). In order to discuss the main assumption of section 6, we first focus on the simple case of Brownian tracer particles (*i.e.* $\beta_x\left(Z\right)=\beta_z\left(Z\right)=1$) that are advected in a linear shear flow, within in a closed channel of thickness H, and in the absence of any electrostatic repulsion ($F_{\mathrm{el}}=0$). We generate 10^4 particle trajectories leaving from initial altitudes described by the uniform distributions defined in the previous section. As such, we consider that the particles are initially located on a line of spatial extent nH. The numerical time step is typically $\delta t=0.001\tau_z$, and the total duration is approximately $10\tau_z$. Reflective boundary conditions are used at the two walls, *i.e.* at $z=0$ and $z=H$. The simulations are performed for the dot ($n=0$), half-line
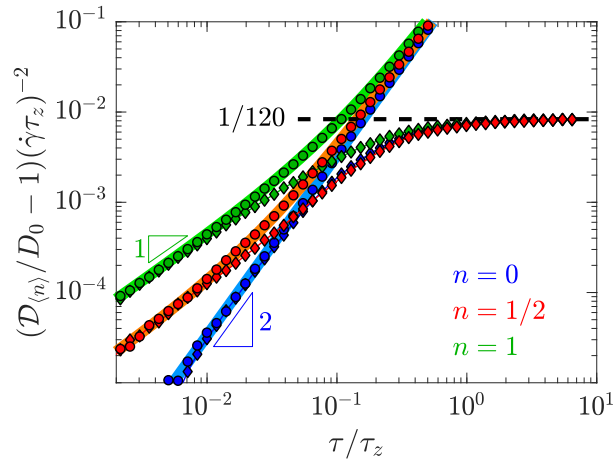
Figure S3: *Reduced dispersion coefficient as a function of dimensionless lag time, from Langevin simulations in free space (circles) and in a confined channel (diamonds), for different initial conditions: dot (blue), half-line (red) and line (green). The coloured plain lines and black dashed line respectively show the theoretical predictions for the short-time (Eq. (S41)) and long-time (Eq. (S19)) limits.*

($n = 1/2$) and line ($n = 1$) conditions. To highlight the relative effect of confinement on the dispersion, we also performed reference simulations in free space (*i.e.* without walls). In all cases, the dispersion coefficient $\mathcal{D}_x$ is calculated from the mean-squared displacement (see section 6) and shown in Fig. S3.

For all conditions, the free-space reduced dispersion coefficient continuously increases with time and is in agreement at all times with the predictions of Eq. (S41). In particular, we clearly observe the expected crossover from the linear to the quadratic behaviours in lag time for particles that are initially broadly distributed in altitudes ($n = 1$).

Furthermore, the Langevin simulation results of the Taylor dispersion in a finite-sized channel are also plotted in Fig. S3. The reduced dispersion coefficients are found to first increase at times shorter than τ_z, following Eq. (S41) as in the free-space case. In contrast to the latter, in the long-time limit, the reduced dispersion coefficient saturates and reaches the constant value predicted by Eq. (S19) no matter the initial particle distribution.

7.3 Effects of hydrodynamic and electrostatic interactions

The previous simulations have been performed without hindered diffusion and electrostatic interactions, which are physical effects that may impact the experiments and that are inherent to nanofluidic settings. We thus performed additional Langevin simulations, including the interactions between the finite-size colloids and the glass wall located at $z = 0$. Simple reflective boundary conditions are maintained at the other boundary, located at $z = H$. The electrostatic parameters were chosen as those that give agreement between the experimental and theoretical SID. Specifically, the particle-wall interaction, ϕ_{el}, is exponentially decaying with magnitude 1.4×10^{-21} J, Debye length 60 nm and thermal energy 4.1×10^{-21} J for input to Eq. S1. Furthermore, at the initial time, the particles are placed in the segments (dot, half-line, line) of the previous section also following the Boltzmann distribution $C(z_c) \propto \exp(-\phi_{el}(z_c)/kT)$. As described by Eqs. (S45) and (S46), we also incorporate non-trivial, hydrodynamic interactions with the wall.

In Fig. S4, we display in red the reduced dispersion coefficients obtained from the Langenvin simulations incorporating electrostatic and hydrodynamic interactions with the wall. These are shown as a function of dimensionless time, using $\tau_z = H^2/D_0$, for all initial conditions. The rescaled dispersion coefficients are found to be systematically smaller than the ones for tracer molecules in finite-sized channels.
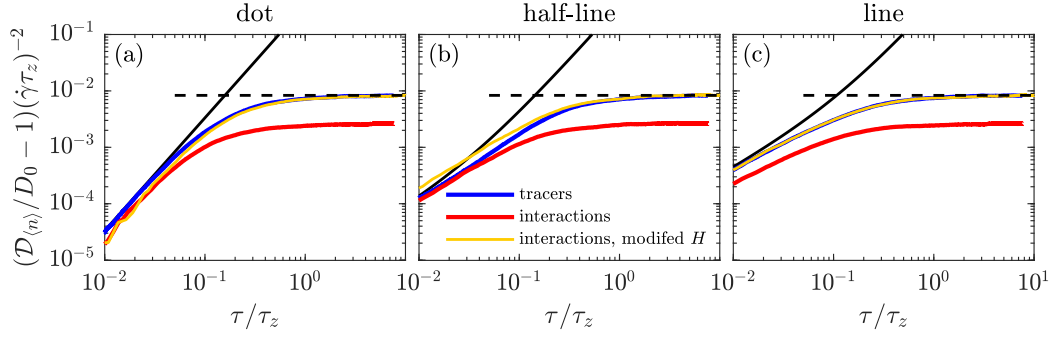
Figure S4: *Reduced dispersion coefficient from (red) Langevin simulations in a channel, including electrostatic repulsion and hindered diffusion induced by the wall located at $z = 0$. These are plotted for three different initial conditions (a,b,c) as a function of dimensionless time. For comparison, we plot the same data (orange) with time on both axes rescaled by the modified time scale $\tau_z = (0.75H)^2/D_0$, and the simulation data of Fig. S3 for (blue) tracer particles in a channel with no interactions with the wall. The lines indicate the asymptotic limits for (horizontal dashed) long times and short times (sloping solid); respectively, a constant value of 1/120 and Eq. 3 in the main paper.*

To justify the difference between tracers and finite-sized, interacting particles, we particularly note that electrostatic forces repel the colloids from the wall, and therefore reduce the area accessible to them. As a secondary effect, the hydrodynamic interactions are thus also reduced since those are maximal at the wall; we will thus assume in the following that D_0 is not modified even while the effect may be slightly operative. As a result of the effectively reduced channel size, the associated timescale should be modified. Therefore, we replot in Fig. S4 the reduced dispersion coefficients versus the dimensionless time by modifying τ_z, using rather $0.75H$, giving a smaller, empirical diffusion time scale $\tau_z = (0.75H)^2/D_0$. We find that the simulation results in the presence of interactions with the wall in an effectively smaller channel of size $0.75\,H$ agree well with the simulation results for tracer particles in the original channel of size H, whatever the initial altitude distributions. This result indicates that the combined effect of electrostatic interactions and hindered diffusion mainly lead – in our experimental range – to a reduced effective time scale τ_z without significantly altering the time dependence itself.

References

[1] Xu Zheng, Fei Shi, and Zhanhua Silber-Li. Study on the statistical intensity distribution (sid) of fluorescent nanoparticles in tirfm measurement. *Microfluidics and Nanofluidics*, 22(11):127, 2018.

[2] Zhenzhen Li, Loïc Deramo, Choongyeop Lee, Fabrice Monti, Marc Yonger, Patrick Tabeling, Benjamin Chollet, Bruno Bresson, and Yvette Tran. Near-wall nanovelocimetry based on total internal reflection fluorescence with continuous tracking. *Journal of Fluid Mechanics*, 766:147–171, 2015.

[3] B Derjaguin. On the repulsive forces between charged colloid particles and on the theory of slow coagulation and stability of lyophobe sols. *Transactions of the Faraday Society*, 35:203–215, 1940.

[4] Evert Johannes Willem Verwey. Theory of the stability of lyophobic colloids. *The Journal of Physical Chemistry*, 51(3):631–636, 1947.

[5] Dennis C Prieve. Measurement of colloidal forces with tirm. *Advances in Colloid and Interface Science*, 82(1-3):93–125, 1999.

[6] AJ Goldman, RG Cox, and H Brenner. Slow viscous motion of a sphere parallel to a plane wallii couette flow. *Chemical Engineering Science*, 22(4):653–660, 1967.

[7] Albert Einstein. Über die von der molekularkinetischen theorie der wärme geforderte bewegung von in ruhenden flüssigkeiten suspendierten teilchen. *Annalen der physik*, 322(8):549–560, 1905.

[8] Geoffrey Ingram Taylor. Dispersion of soluble matter in solvent flowing slowly through a tube. *Proceedings of the Royal Society of London. Series A. Mathematical and Physical Sciences*, 219(1137):186–203, 1953.

[9] TGM Van de Ven. Diffusion of brownian particles in shear flow. *Journal of Colloid and Interface Science*, 62(2):352–355, 1977.

[10] GK Batchelor. Mass transfer from a particle suspended in fluid with a steady linear ambient velocity distribution. *Journal of Fluid Mechanics*, 95(2):369–400, 1979.

[11] RT Foister and TGM Van De Ven. Diffusion of brownian particles in shear flows. *Journal of Fluid Mechanics*, 96(1):105–132, 1980.

[12] C Van den Broeck, JM Sancho, and M San Miguel. Harmonically bound brownian motion in flowing fluids. *Physica A: Statistical Mechanics and its Applications*, 116(3):448–461, 1982.

[13] Kunimasa Miyazaki and Dick Bedeaux. Brownian motion in a fluid in simple shear flow. *Physica A: Statistical Mechanics and its Applications*, 217(1-2):53–74, 1995.

[14] Hiroshi Orihara and Yoshinori Takikawa. Brownian motion in shear flow: Direct observation of anomalous diffusion. *Physical Review E*, 84(6):061120, 2011.

[15] Einar Orn Fridjonsson, Joseph D Seymour, and Sarah L Codd. Anomalous preasymptotic colloid transport by hydrodynamic dispersion in microfluidic capillary flow. *Physical Review E*, 90(1):010301, 2014.

[16] Yoshinori Takikawa, Takahiro Nunokawa, Yuji Sasaki, Makoto Iwata, and Hiroshi Orihara. Three-dimensional observation of brownian particles under steady shear flow by stereo microscopy. *Physical Review E*, 100(2):022102, 2019.

[17] Donald L Ermak and J Andrew McCammon. Brownian dynamics with hydrodynamic interactions. *The Journal of chemical physics*, 69(4):1352–1360, 1978.

[18] Luc P Faucheux and Albert J Libchaber. Confined brownian motion. *Physical Review E*, 49(6):5158, 1994.